532 *Chem. Mater.* **2010,** *22,* 532–540
DOI:10.1021/cm903170t

CHEMISTRY OF
MATERIALS
Article

Structures, Phase Transitions, Hydration, and Ionic Conductivity of $Ba_4Ta_2O_9$

Chris D. Ling,*[†,‡] Maxim Avdeev,[‡] Vladislav V. Kharton,[§] Aleksey A. Yaremchenko,[§] René B. Macquart,[†,‡] and Markus Hoelzel[⊥]

[†]*School of Chemistry, The University of Sydney, Sydney 2006, Australia,* [‡]*Bragg Institute, ANSTO, PMB 1, Menai 2234, Australia,* [§]*Department of Ceramics and Glass Engineering, CICECO, University of Aveiro, 3810-193 Aveiro, Portugal, and* [⊥]*Darmstadt University of Technology, Petersenstrasse 23, D-64287 Darmstadt, Germany*

Received October 15, 2009. Revised Manuscript Received December 2, 2009

Low-temperature α-$Ba_4Ta_2O_9$ is isostructural with α-$Ba_4Nb_2O_9$ ($Sr_4Ru_2O_9$ type), and it undergoes a reconstructive phase transition at approximately the same temperature (1400 K) to a γ form that can easily be quenched to room temperature. However, the γ forms of the two compounds are completely different. Whereas γ-$Ba_4Nb_2O_9$ represents a unique structure type, γ-$Ba_4Ta_2O_9$ adopts a more conventional 6H-perovskite type. The $\alpha \rightarrow \gamma$ transition is virtually irreversible in the tantalate, unlike the niobate, which can be converted back to the α form by annealing slightly below the transition temperature. Quenched γ-$Ba_4Ta_2O_9$ is highly strained due to the extreme size mismatch between Ba^{2+} (1.35 Å) and Ta^{5+} (0.64 Å) cations in perovskite B-sites, and undergoes a series of symmetry-lowering distortions from $P6_3/mmc \rightarrow P6_3/m \rightarrow P2_1/c$; the second of these transitions has not previously been observed in a 6H perovskite. Below ~950 K, both α-$Ba_4Ta_2O_9$ and γ-$Ba_4Ta_2O_9$ hydrate to a greater extent than the corresponding phases of $Ba_4Nb_2O_9$. Both hydrated forms show significant mixed protonic and oxide ionic conductivity, and electronic conductivity upon dehydration.

Introduction

Materials that exhibit significant mobility of several different types of charge carriers (e.g., oxide ions, protons, and electrons) have diverse potential applications as fuel-cell membranes, electrodes, batteries, and sensors. New mixed conductors are of perennial interest, especially when they are stable over wide ranges of temperature and redox conditions. Several niobium and tantalum oxides have recently been shown to exhibit promising mixed conductivity associated with a surprisingly high uptake of protons at moderate temperatures (below ~600 °C). These include La(Nb,Ta)O_4,[1−3] $Ba_3Ca_{1+x}(Nb,Ta)_{2-x}O_{9-3x/2}$,[4−6] HLa(Nb,Ta)$_2O_7\cdot 0.5H_2O$,[7] and La_3(Nb,Ta)O_7.[8] The niobates and tantalates are isostructural, in most cases (the exception being $LaNbO_4$ versus $LaTaO_4$), with the niobates generally being the better conductors, because of the fact that Nb is more easily reduced from its standard 5+ oxidation state than is Ta.

We recently added $Ba_4Nb_2O_9$[9−13] to the list of proton-conducting niobates.[14] This compound has two basic polymorphs: a high-temperature γ phase, with a unique structure type; and a low-temperature α phase, with the $Sr_4Ru_2O_9$ structure type. The phases are separated by a reconstructive transition at ~1370 K, the kinetics of which are sufficiently slow, such that the γ phase can easily be quenched to room temperature. Below ~950 K, both α and γ phases absorb significant amounts of water. In the case of the γ phase, protons from absorbed water occupy ordered positions in the structure, giving rise to a series of stoichiometric phases: γ-III ($Ba_4Nb_2O_9\cdot {}^1/_3H_2O$) at room temperature, γ-II ($Ba_4Nb_2O_9\cdot {}^1/_6H_2O$) above ~760 K, and γ-I ($Ba_4Nb_2O_9$) above ~950 K. The hydrated γ phases exhibit particularly fast protonic and oxide ionic transport, because of the presence of two-dimensional (2D) layers containing Nb^{5+} cations with

---

*Author to whom correspondence should be addressed. E-mail: c.ling@chem.usyd.edu.au.

(1) Haugsrud, R.; Norby, T. *J. Am. Ceram. Soc.* **2007**, *90*(4), 1116–1121.
(2) Haugsrud, R.; Norby, T. *Solid State Ionics* **2006**, *177*(13−14), 1129–1135.
(3) Haugsrud, R.; Norby, T. *Nat. Mater.* **2006**, *5*(3), 193–196.
(4) Du, Y.; Nowick, A. S. *Solid State Ionics* **1996**, *91*(1−2), 85–91.
(5) Nowick, A. S.; Du, Y. *Solid State Ionics* **1995**, *77*, 137–146.
(6) Liang, K. C.; Du, Y.; Nowick, A. S. *Solid State Ionics* **1994**, *69*(2), 117–120.
(7) Kobayashi, Y.; Schottenfeld, J. A.; Macdonald, D. D.; Mallouk, T. E. *J. Phys. Chem. C* **2007**, *111*(7), 3185–3191.
(8) Haugsrud, R.; Risberg, T. *J. Electrochem. Soc.* **2009**, *156*(4), B425–B428.
(9) Bezjak, J.; Jancar, B.; Recnik, A.; Suvorov, D. *J. Eur. Ceram. Soc.* **2008**, *28*(14), 2771–2776.
(10) Bezjak, J.; Recnik, A.; Jankcar, B.; Boullay, P.; Evans, I. R.; Suvorov, D. *J. Am. Ceram. Soc.* **2009**, *92*(8), 1806–1812.
(11) Blasse, G. *J. Inorg. Nucl. Chem.* **1965**, *27*(5), 993–1003.
(12) Leshchenko, P. P.; Lykova, L. N.; Kovba, L. M.; Stefanovich, S. Y.; Chechkin, V. V. *Inorg. Mater.* **1985**, *21*(2), 227–230.
(13) Leshchenko, P. P.; Paromova, M. V.; Lykova, L. N.; Kovba, L. M. *Vestn. Mosk. Univ. Ser. 2: Khim.* **1979**, *20*(2), 148–151.
(14) Ling, C. D.; Avdeev, M.; Kutteh, R.; Kharton, V. V.; Yaremchenko, A. A.; Fialkova, S.; Sharma, N.; Macquart, R. B.; Hoelzel, M.; Gutmann, M. J. *Chem. Mater.* **2009**, *21*, 3853–3864.

unusually low oxygen coordination numbers (4 or 5) separated by discrete OH groups. Hydration seems to play an important role in stabilizing the γ phases at low temperatures, with the $\gamma \rightarrow \alpha$ transition on reheating a quenched sample occurring at higher temperatures in humid atmospheres.

This report concerns $Ba_4Ta_2O_9$, which clearly has a close chemical relationship to $Ba_4Nb_2O_9$. Previous reports suggest that $Ba_4Ta_2O_9$ undergoes a similar reconstructive phase transition at a similar temperature. It was first synthesized in 1965 by Blasse,[11] who reported that its structure was complex but probably a distorted variant of 6H-type hexagonal perovskite ($BaTiO_3$ type). Apart from a brief mention by Kemmler-Sack et al.[15] as a high-temperature phase with an orthorhombically distorted hexagonal perovskite structure, the only other significant reports in the literature were by Leschenko et al.[16–18] On the basis of powder X-ray diffraction (XRD) patterns from quenched samples, and thermogravimetric analysis (TGA), they reported three phases: a high-temperature form, α-$Ba_4Ta_2O_9$ ($T > 1370$ K) with hexagonal $P\bar{3}m1$ space group symmetry, $a = 5.952$, $c = 4.253$ Å; an intermediate-temperature form β-$Ba_4Ta_2O_9$ ($1240 < T < 1370$ K) with a hexagonal $2a$, $4c$ superstructure of the α-form, $a = 12.19$ Å, $c = 16.12$ Å; and a low-temperature form γ-$Ba_4Ta_2O_9$ ($T < 1240$ K) with orthorhombic $C222_1$ space group symmetry, $a = 12.15$ Å, $b = 21.16$ Å, $c = 16.07$ Å. Note that these labels are essentially the reverse of those used by Leschenko et al. for $Ba_4Nb_2O_9$,[12,13] for which they labeled the low-temperature phase "α" and the high-temperature phase "γ". This is rather confusing, given that the unit cells and symmetries suggest that the low- and high-temperature forms of the two compounds are isostructural. Therefore, we propose at the outset to relabel the low-temperature form as α-$Ba_4Ta_2O_9$ and the high-temperature form as γ-$Ba_4Ta_2O_9$, for consistency with the more-significant body of literature on $Ba_4Nb_2O_9$.

The aim of this investigation was to solve and refine the various crystal structures of $Ba_4Ta_2O_9$ and to characterize their physical properties—especially their conductivity and hydration properties—given our recent findings for $Ba_4Nb_2O_9$.

Experimental Methods

Single-phase polycrystalline samples of the low-temperature form α-$Ba_4Ta_2O_9$ were prepared by solid-state synthesis in air from $BaCO_3$ and Ta_2O_5 (99.99% purity or greater). Prior to weighing, $BaCO_3$ was dried at 1000 K overnight and Ta_2O_5 was annealed in air at 1370 K for 2 h. The stoichiometric mixture was ground in an agate mortar and pestle and annealed in air at 1320 K for 20 h with several regrindings and then ball-milled. Single-phase polycrystalline samples of the high-temperature form γ-$Ba_4Ta_2O_9$ were prepared by heating approximately half of the α-$Ba_4Ta_2O_9$ sample (~10 g) to 1620 K for 20 h in air in a platinum crucible, cooling to 1470 K, then removing it from the furnace and quenching it on a steel plate.

Ceramic samples of α-$Ba_4Ta_2O_9$ were prepared for conductivity measurements by uniaxial pressing of disk- and bar-shaped green compacts at 300 MPa and sintering them at 1320 K for 20 h in air. The samples of γ-$Ba_4Ta_2O_9$ were pressed in the same manner and sintered at 1820 K for 10 h in air, then quenched from 1470 K. The density of the α-$Ba_4Ta_2O_9$ pellets was determined to be 4.50 g/cm^3 (or 57% of the theoretical density), whereas that of the γ-$Ba_4Ta_2O_9$ pellets was determined to be 6.50 g/cm^3 (or 83% of the theoretical density) (both densities are based on the structural models presented below). Although a series of attempts to prepare α-$Ba_4Ta_2O_9$ with a higher density were made via annealing of sintered γ-$Ba_4Ta_2O_9$ at 1300–1350 K during 100–150 h, the resultant ceramics always contained the γ phase, because of stagnated kinetics of the $\gamma \rightarrow \alpha$ transition, as briefly discussed below; further densification of γ-$Ba_4Ta_2O_9$ via sintering at 1870–1920 K was also impossible, because of fast grain growth, leading to insufficient mechanical strength.

Room-temperature XRD data were collected on a Panalytical X'Pert Pro diffractometer using Cu Kα radiation. High-temperature synchrotron XRD (S-XRD) data were collected at the Powder Diffraction Beamline of the Australian Synchrotron at $\lambda = 0.82563$ Å; samples were placed in unsealed 1-mm-diameter quartz capillaries and heated with a hot air blower to 1150 K over 12 h, with data collected at 25-K intervals.

Room-temperature neutron powder diffraction (NPD) data were collected on the instrument Echidna at the OPAL reactor (Lucas Heights, Australia) at $\lambda = 1.6215$ and 2.4395 Å; samples were placed in 9-mm-diameter vanadium cans and data collected over 4 h per sample. High-temperature NPD data were collected on the SPODI instrument at the FRM-II research reactor (Garching, Germany) at $\lambda = 1.5482$ Å; samples were placed in 8-mm-diameter sealed niobium cans and heated up to 1470 K with a cylindrical niobium element, while complete datasets were collected over 1–6 h each at selected temperatures.

Differential thermal analysis (DTA) data were collected on a Setaram LabSys TG-DTA16 instrument (heating rate of 2 K/min) in air. Thermogravimetric analysis (TGA) data were collected on a Setaram SetSys 16/18 instrument (heating/cooling rate of 2 K/min; sensitivity of 0.4 μg; initial sample weights of 0.8–1.1 g) in flowing dry air.

The total (ionic + electronic) conductivity (σ) was determined by AC impedance spectroscopy (Hewlett–Packard Model HP4284A precision LCR meter, 20 Hz–1 MHz) at temperatures below ~1270 K, and a four-probe DC technique at temperatures above ~1270 K, in air and in argon. The gas flows were dried by passing them through silica gel or humidified by bubbling through water. Water vapor partial pressures were measured by a Jumo humidity transducer. The criterion for equilibration after a change in either oxygen pressure or temperature included the relaxation of the sample resistance less than 0.5% during 30 min.

The oxygen-ion ($\bar{t}_O$) and proton ($\bar{t}_H$) transference numbers for γ-$Ba_4Ta_2O_9$, averaged under an oxygen and/or water vapor partial pressure gradient, in dry and wet atmospheres, were determined by the electromotive force (EMF) method. The experimental setup (see Figure 1) comprised one disk-shaped sample with porous platinum electrodes, hermetically sealed onto 8-mol % yttria-stabilized zirconia (8YSZ) tube. Three

---

(15) Kemmler-Sack, S.; Thumm, I.; Herrmann, M. *Z. Anorg. Allg. Chem.* **1981**, *479*(8), 177–183.

(16) Kovba, L. M.; Lykova, L. N.; Paromova, M. V.; Lopato, L. M.; Shevchenko, A. V. *Russ. J. Inorg. Chem.* **1977**, *22*(10), 1544–1546.

(17) Paromova, M. V.; Leshchenko, P. P.; Lykova, L. N.; Kovba, L. M. *Vestn. Mosk. Univ. Ser. 2: Khim.* **1976**, *17*(4), 499–501.

(18) Spitsyn, V. I.; Ippolitova, E. A.; Kovba, L. M.; Lykova, L. N.; Leshchenko, P. P. *Russ. J. Inorg. Chem.* **1982**, *27*(4), 827–832.

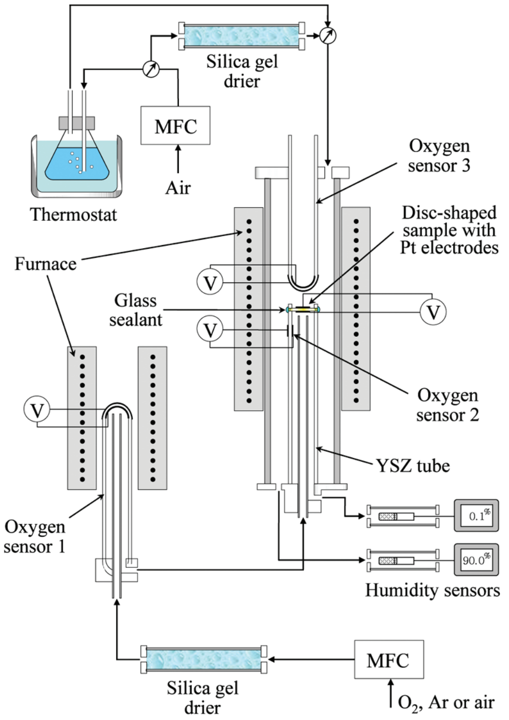

Figure 1. Schematic outline of the experimental setup used for the electromotive force (EMF) measurements in dry and wet atmospheres; the acronym "MFC" denotes the mass flow controller.

8YSZ oxygen sensors were used to control the oxygen chemical potential in the inlet gases and near the electrodes. Dried oxygen, Ar/O_2 mixtures, or air were supplied onto one electrode, while another electrode was exposed to the flow of dried or humidified air. The measurements were performed at 973−1223 K. The average transference numbers were calculated from the EMF of the concentration cells ($E_{\mathrm{II-I}}$) as

$$E_{\mathrm{II-I}} = (\bar{t}_{\mathrm{O}} + \bar{t}_{\mathrm{H}})\left(\frac{RT}{4F}\right) \ln \left(\frac{p_{\mathrm{O_2}}^{\mathrm{II}}}{p_{\mathrm{O_2}}^{\mathrm{I}}}\right) - \bar{t}_{\mathrm{H}}\left(\frac{RT}{2\mathrm{F}}\right) \ln \left(\frac{p_{\mathrm{H_2O}}^{\mathrm{II}}}{p_{\mathrm{H_2O}}^{\mathrm{I}}}\right)$$

where p is the partial pressure of the given component. Here, the hydrogen-containing charge carriers are assumed to be exclusively protons, in agreement with the electromotive force (EMF) sign in the water vapor concentration cells, where the oxygen partial pressures at the electrodes were equal to each other ($p_{\mathrm{O_2}}{}^{\mathrm{II}} = p_{\mathrm{O_2}}{}^{\mathrm{I}}$). The oxygen ionic contribution was estimated by fixing the water vapor partial pressures at the electrodes ($p_{\mathrm{H_2O}}^{\mathrm{II}} = p_{\mathrm{H_2O}}^{\mathrm{I}}$).

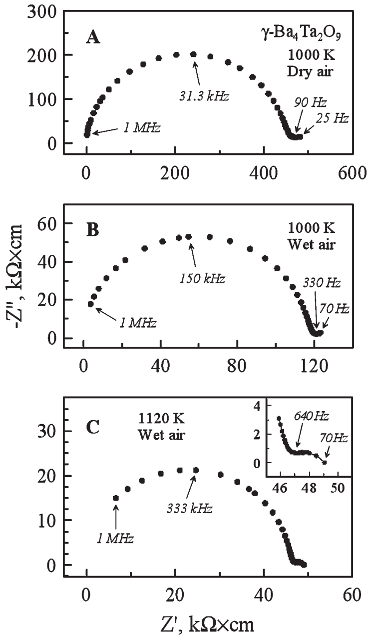

Figure 2. Impedance spectra of $Ba_4Ta_2O_9$ ceramics with porous platinum electrodes in (A) dry air and (B and C) wet air, where the partial pressure of water vapor is ∼50 Pa and ∼3.5 kPa, respectively. Note that the weak electrode signal confirms a presence of mixed conductivity with significant ionic contribution, both in dry air and in wet air.

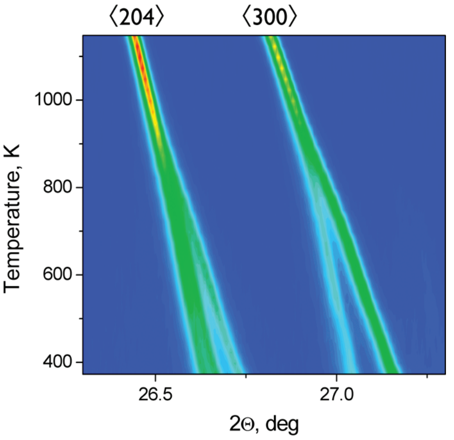

Figure 3. Thermodiffractogram showing part of the S-XRD (λ = 0.82563 Å) patterns of quenched γ-$Ba_4Ta_2O_9$ collected on heating, showing that the symmetry is reduced from hexagonal to monoclinic at < 900 K. Indexing of peaks corresponds to the hexagonal $a \approx 6.1$ Å, $c \approx 16.1$ Å high-temperature cell.

Notice that, although the use of the classical EMF method results in large experimental uncertainties when mass transport through the mixed-conducting membrane and the resultant electrode-polarization phenomena are significant,[19] these factors were found negligible in the present case, bceause of the high electrical resistivity of $Ba_4Ta_2O_9$ ceramics (see Figure 2). In particular, the electrolytic permeation fluxes in the concentration cells were determined to be comparable to or below the sensitivity limit; the corresponding values expressed in electrical units are < 4 μA/cm^2 at 1223 K and <0.5 μA/cm^2 at 973 K. The same conclusion was drawn analyzing the impedance spectra, which show that the electrode polarization resistance in the present case is much smaller, compared to the ohmic resistance (e.g., see the inset in Figure 2C). The error in $\bar{t}_{\mathrm{O}}$ and $\bar{t}_{\mathrm{H}}$ values, estimated from the reproducibility tests using ceramic membranes with different thicknesses, varied in the range from ±0.02 to ±0.04. The use of modified measurement methods[19] was associated with larger uncertainties due to shifting $p_{\mathrm{O_2}}$ and/or $p_{\mathrm{H_2O}}$ values at the membrane electrodes and a higher noise level in the DC regimes, again because of the high total resistivity. While the cumulative errors achieved a value of ±0.1, the estimated transference numbers were similar to the data collected by the classical EMF technique within these limits of experimental uncertainty.

Results

1. Temperature-Dependent Phase Transitions. XRD of our polycrystalline samples confirmed that γ-$Ba_4Ta_2O_9$ is

---

[19] Kharton, V. V.; Marques, F. M. B. *Solid State Ionics* **2001**, *140* (3−4), 381–394.

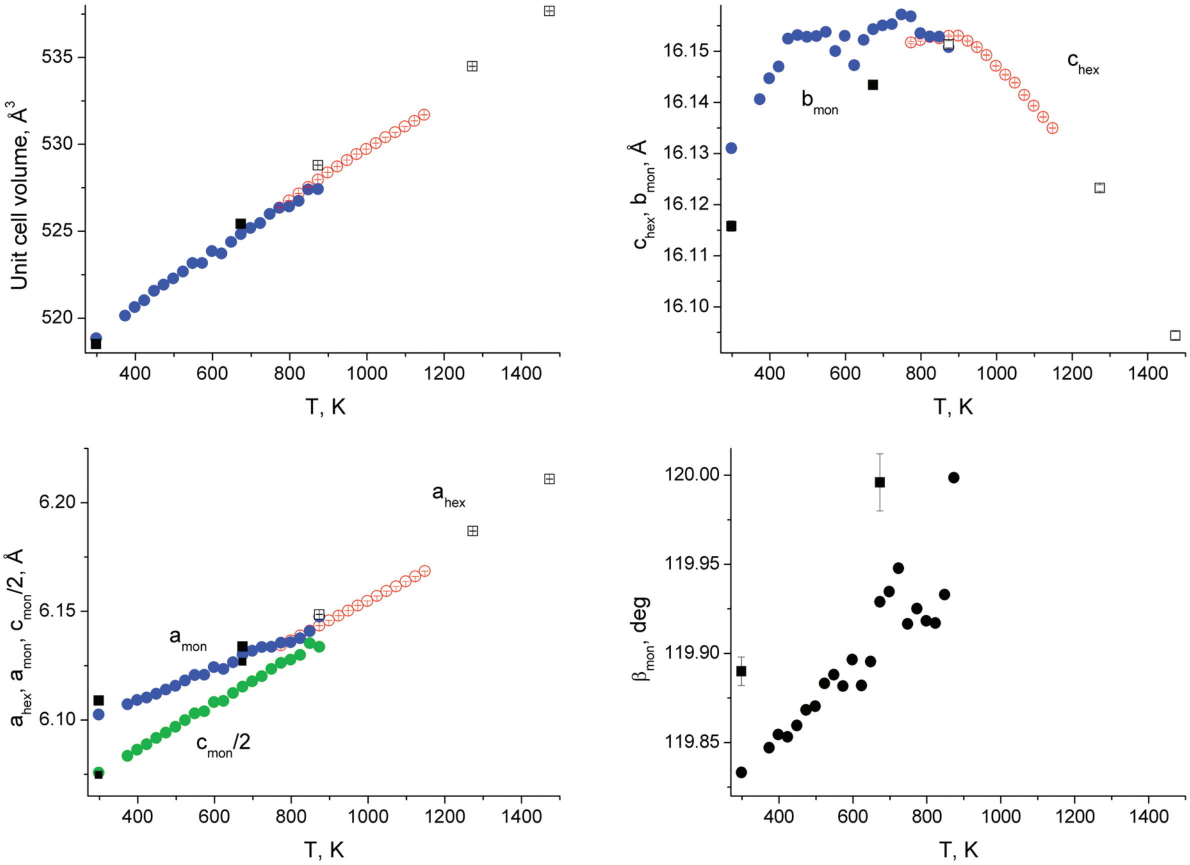

Figure 4. Evolution of the subcell lattice parameters of quenched γ-$Ba_4Ta_2O_9$ on heating, as determined by Le Bail fits to S-XRD and NPD data. Solid and open symbols indicate monoclinic and hexagonal modifications, respectively. Circles and squares indicate results extracted from synchrotron and neutron diffraction data (SPODI), respectively.

easily obtained by quenching from >1400 K, while α-$Ba_4Ta_2O_9$ is obtained by synthesis at <1320 K. Unlike $Ba_4Nb_2O_9$, reannealing of the γ phase below 1400 K did not result in reconversion to the α form, even after several days. Differential thermal analysis (DTA) studies showed an endothermal effect corresponding to the $\alpha\rightarrow\gamma$ transition on heating in air at 1403 ± 10 K. However, due to kinetically stagnated phase changes, this process was found to be almost irreversible; and annealing γ-$Ba_4Ta_2O_9$ ceramics at 1350 K for 120 h did not result in the $\gamma\rightarrow\alpha$ transformation, according to XRD. Note that these stagnated kinetics may lead to significant errors in determination of the phase-transition temperature.

To investigate the intermediate-temperature form β-$Ba_4Ta_2O_9$ reported by Leschenko et al.[16−18] as a superstructure of the high-temperature form, we performed an *in situ* high-temperature S-XRD experiment on our quenched γ-$Ba_4Ta_2O_9$ sample. Part of the S-XRD patterns is shown in Figure 3. Above 900 K, the pattern can be indexed to a hexagonal unit cell with dimensions of $a \approx 6.1$ Å and $c \approx 16.1$ Å, which is clearly related to the hexagonal cells reported by Leschenko et al. for the high-temperature form ($a = 5.952$ Å, $c = 4.253$ Å) and intermediate-temperature form ($a = 12.19$ Å, $c = 16.12$ Å). Below 900 K, we observe peak splitting, which is indicative of symmetry reduction to monoclinic.

This structural transition was also investigated in an *in situ* high-temperature NPD experiment on SPODI. NPD has certain advantages over XRD in this context: neutrons can easily penetrate the thick walls of a furnace required to homogeneously heat a sample to >1400 K, allowing us to study the $\alpha\rightarrow\gamma$ and $\gamma\rightarrow\alpha$ transitions; and neutron diffraction is far more sensitive to O atoms in the presence of heavy metals such as barium and tantalum. Data were collected while slowly heating samples of α-$Ba_4Ta_2O_9$ and quenched γ-$Ba_4Ta_2O_9$ from room temperature to 1470 K. As for our differential thermal analysis (DTA) and XRD results previously discussed, the $\alpha\rightarrow\gamma$ transition was clearly observed on a time scale of hours, but the $\gamma\rightarrow\alpha$ transition was not observed at all, even after several hours.

Neither our XRD from quenched samples, nor our high-temperature S-XRD or NPD data, show evidence for a discrete intermediate-temperature β form. Rather, they suggest that the quenched high-temperature γ form undergoes a conventional second-order symmetry-reducing transition at ~900 K. The evolution of the (subcell) lattice parameters and volume from room temperature to 1470 K (obtained by Le Bail fits to S-XRD and NPD data) for quenched γ-$Ba_4Ta_2O_9$ through this transition is shown in Figure 4. Note the unusual broad maximum of the *b*-axis (equivalent to the hexagonal *c*-axis) at ~500−900 K, which was observed to be reproducible in

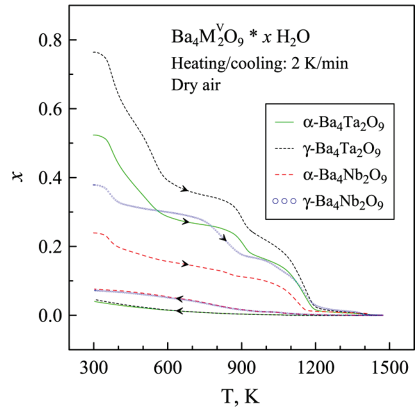

Figure 5. Variations of the water content in powdered $Ba_4Ta_2O_9$ and $Ba_4Nb_2O_9$[14] samples on heating and then cooling in air at $p_{H_2O} \approx 50$ Pa, as calculated from TGA data, assuming that the samples contain no water at 1470 K and are oxygen-stoichiometric. (Note that additional water uptake at low temperatures, e.g., below ~400 K, is typical for mixed-oxide/proton conductors, because of surface decomposition and water incorporation at grain boundaries).

a subsequent variable-temperature laboratory XRD experiment and show no hysteresis on cooling. The volume coefficient of thermal expansion (CTE), which is approximately linear over the entire range measured, was calculated as $\beta = 3.15 \times 10^{-5}\ K^{-1}$.

2. Hydration Behavior. We carefully investigated the hydration behavior of $Ba_4Ta_2O_9$, in light of the ordered hydration that we observed in $Ba_4Nb_2O_9$,[14] as well as other recent reports of hydration and proton conduction in niobates. Figure 5 shows TGA data confirming the existence of stable hydrated phases of both α-$Ba_4Ta_2O_9$ and γ-$Ba_4Ta_2O_9$ at room temperature and ~700 K, compared directly to the same data for $Ba_4Nb_2O_9$. The data unambiguously show that the tantalum-containing analogue absorbs larger amount of water. They also show that, as for $Ba_4Nb_2O_9$, the high-temperature γ form of $Ba_4Ta_2O_9$ absorbs a larger amount of water than the low-temperature α form.

3. Structure Solution and Refinement. The structure of α-$Ba_4Ta_2O_9$ was determined to be $Sr_4Ru_2O_9$-type,[20] which was entirely analogous with that of α-$Ba_4Nb_2O_9$. This is a partially disordered structure consisting of Ta_2O_9 face-sharing octahedral dimers, which are aligned with the *c*-axis and separated by voids almost as large as the dimers themselves. The structure is partially disordered because there are four possible positions for these dimers along the *c*-axis, but only three crystallographically distinct sites. The final Rietveld-refined structure is shown in Figure 6, drawn using the program VESTA.[21] The final Rietveld-refined fit to room-temperature SPODI data using the GSAS software package[22] with the EXPGUI front end[23] is shown in Figure 7, with the refinement data and structural details summarized in Table 1. Some small deficiencies in the Rietveld fit may be indicative of partial ordering of the frustrated columns of Ta_2O_9 dimers, although no long-range-ordered model could be found that significantly improved the fit. Full structural details including bond lengths are included in the CIF file deposited in the Supporting Information.

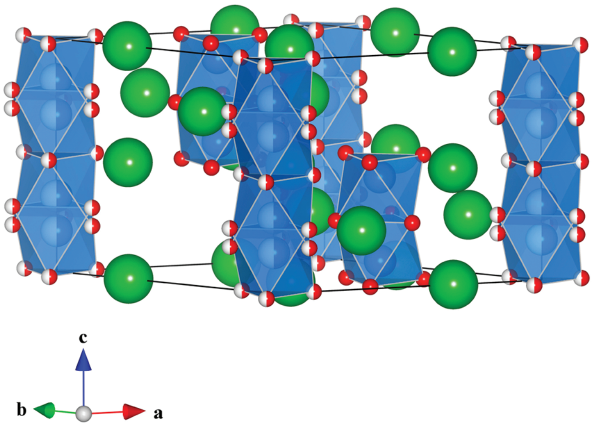

Figure 6. Structure of the low-temperature phase α-$Ba_4Ta_2O_9$ at room temperature, Rietveld-refined against NPD (SPODI) data. Ba atoms are green, Ta atoms are blue, and O atoms are red. Half-occupied sites are represented by half-colored spheres. Note the large voids between Ta_2O_9 octahedral dimers.

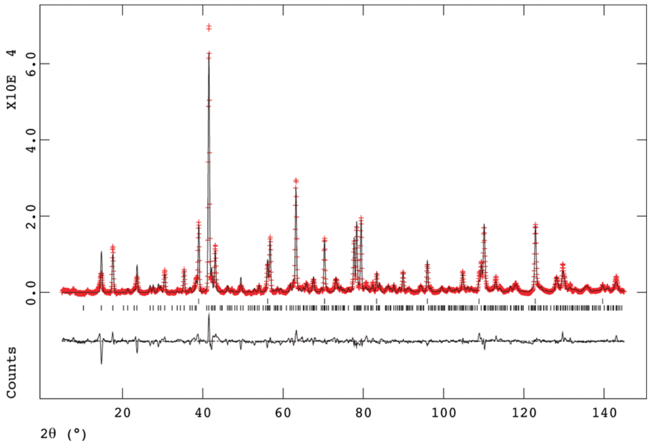

Figure 7. Observed (crosses), calculated (solid line), and difference (below) NPD (SPODI, $\lambda = 1.5482$ Å) profiles for the final Rietveld refinement of α-$Ba_4Ta_2O_9$ at room temperature. The upper row of peak markers indicates peaks due to the niobium sample can.

Table 1. Structural Details for α-$Ba_4Ta_2O_9$ at 300 K, Rietveld-Refined against NPD Data (SPODI, $\lambda = 1.5482$ Å)[a]

atom	*x* (*a*) [Å]	*y* (*b*) [Å]	*z* (*c*) [Å]	$100U_{iso}$ [Å^2]
Ba1	0.6698(17)	0	0	1.06(18)
Ba2	0.3351(19)	0.0091(8)	1/4	2.0(2)
Ta1	0	0	0.175(2)	$2.85(11)^1$
Ta2	2/3	1/3	0.4300(9)	$2.85(11)^1$
O1	0.6738(11)	0.4976(10)	0.5168(5)	$2.78(7)^2$
O2	0.5142(13)	0.3476(11)	1/4	$2.78(7)^2$
O3	0.0000(14)	0.8362(17)	0.7107(13)	$2.78(7)^2$
O4	0.148(2)	0	0	$2.78(7)^2$

[a] Space group: hexagonal $P\bar{6}2c$ (No. 190); $a = 10.2690(3)$ Å and $c = 8.4729(4)$ Å. Overall powder *R*-factors: $R_p = 0.0757$, $wR_p = 0.0957$, $R(F^2) = 0.1264$. Superscript symbols indicate constraints.

---

(20) Dussarrat, C.; Fompeyrine, J.; Darriet, J. *Eur. J. Solid State Inorg. Chem.* **1995**, *32*(1), 3–14.
(21) Momma, K.; Izumi, F. *J. Appl. Crystallogr.* **2008**, *41*(3), 653–658.
(22) Larson, A. C.; von Dreele, R. B. *GSAS: The General Structure Analysis Program*; Los Alamos National Laboratory: Los Alamos, NM, 1990.
(23) Toby, B. H. *J. Appl. Crystallogr.* **2001**, *34*, 210–213.

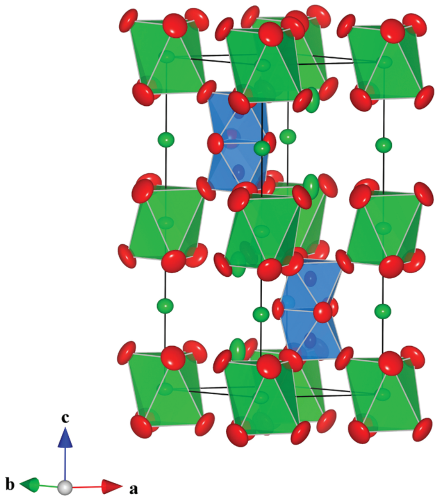

Figure 8. Structure of γ-$Ba_4Ta_2O_9$ at 1270 K, in $P6_3/m$ space group symmetry, Rietveld-refined against NPD (SPODI) data. Note the slight relative rotation of TaO_6 octahedra about the *c*-axis in successive layers, associated with the symmetry reduction from ideal $P6_3/mmc$. Ba atoms are green, Ta atoms are blue, and O atoms are red. Ellipsoids show anisotropic ADPs at 50% probability.

Structure solution and characterization of γ-$Ba_4Ta_2O_9$ began by examining high-temperature NPD (SPODI) data in the thermodynamically stable regime above 1400 K. After careful comparisons with known structures in chemically related systems, we determined that γ-$Ba_4Ta_2O_9$ has a 6H-perovskite ($BaTiO_3$-type) structure. Above 900 K, the space group symmetry is $P6_3/m$, which is derived from the ideal 6H-perovskite space group symmetry $P6_3/mmc$ by octahedral rotations about the *c*-axis. This symmetry-reducing mode is also observed in the closely related compound $Ba_3SrTa_2O_9$.[24] No evidence was found for ordered proton or hydroxide sites, such as those observed for γ-$Ba_4Nb_2O_9$;[25] nor is there any obvious location for such sites.

The final structural model for γ-$Ba_4Ta_2O_9$ in $P6_3/m$, Rietveld refined against 1270 K NPD data, is shown in Figure 8. The final Rietveld-refined fit is shown in Figure 9, with the refinement data and structural details summarized in Table 2. The large ADPs (atomic displacement parameters) are due to thermal vibrations at 1270 K. Full structural details including bond lengths are included in the CIF file deposited in the Supporting Information.

S-XRD data for γ-$Ba_4Ta_2O_9$ at room temperature were successfully indexed using a monoclinic cell clearly related to the high-temperature hexagonal modification, i.e., $a_{\text{mon}} \approx a_{\text{hex}}$, $b_{\text{mon}} \approx c_{\text{hex}}$, $c_{\text{mon}} \approx 2a_{\text{hex}}$, $\beta \approx 120°$. Systematic absences of $h0l$ ($l = 2n + 1$) and $0k0$ ($k = 2n + 1$) diffraction peaks and the ratio of the number of observed and calculated reflections pointed to the $P2_1/c$ space group. Symmetry reduction from $P6_3/m$ to $P2_1/c$ was consistent with a group theoretical analysis performed using the program SUBGROUPGRAPH[26] at the Bilbao Crystallographic Server.[27,28] The following Rietveld analysis of the neutron diffraction data collected using the Echidna instrument confirmed the correctness of the choice of space group.

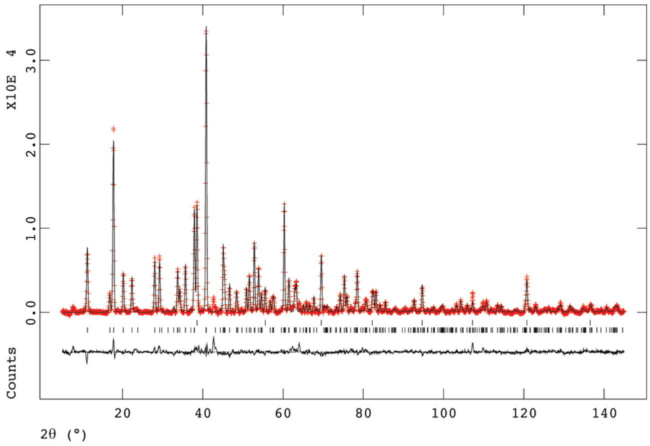

Figure 9. Observed (crosses), calculated (solid line), and difference (below) NPD (SPODI, λ = 1.5482 Å) profiles for the final Rietveld refinement of γ-$Ba_4Ta_2O_9$ in $P6_3/m$ at 1270 K. The upper row of peak markers indicates peaks due to the niobium sample can.

The difference between the low-temperature monoclinic modification of γ-$Ba_4Ta_2O_9$ and its high-temperature hexagonal form is mainly due to cooperative rotation of Ta_2O_9 dimers and distortions of oxygen polyhedra around Ba atoms, as illustrated in Figure 10. Similar behavior has been observed for other $Ba_3AM_2O_9$ perovskites.[25,29]

The final Rietveld-refined fit is shown in Figure 11, with refinement data and structural details summarized in Table 3. Full structural details including bond lengths are included in the CIF file deposited in the Supporting Information.

4. Transport Properties. The impedance spectra of γ-$Ba_4Ta_2O_9$ (recall Figure 2) clearly indicated, in particular, a significant role of protonic transport as the total resistivity decreases under humid conditions. The temperature dependencies of the total conductivity of $Ba_4Ta_2O_9$ ceramics in different atmospheres are compared in Figure 12. All data were collected on cooling in flowing gases. The results show that α-$Ba_4Ta_2O_9$ exhibits mixed ionic and electronic conductivity. The electronic component is *p*-type, as indicated by the conductivity decrease when the oxygen partial pressure decreases. The ionic component may include protonic and, possibly, oxide ionic contributions. The latter is indicated by the fact that the conductivity of α-$Ba_4Ta_2O_9$ in the high-temperature range is essentially independent of partial pressure of water vapor. For γ-$Ba_4Ta_2O_9$, the conductivity in wet atmospheres seems to be essentially protonic in the intermediate- and low-temperature ranges ($T \leq 1000$ K).

---

(24) Zandbergen, H. W.; Ijdo, D. J. W. *Acta Crystallogr., Sect. C: Cryst. Struct. Commun.* **1983**, *39*(JUL), 829–832.

(25) Ling, C. D.; Rowda, B.; Avdeev, M.; Pullar, R. *J. Solid State Chem.* **2009**, *182*(3), 479–483.

(26) Ivantchev, S.; Kroumova, E.; Madariaga, G.; Perez-Mato, J. M.; Aroyo, M. I. *J. Appl. Crystallogr.* **2000**, *33*, 1190–1191.

(27) Aroyo, M. I.; Kirov, A.; Capillas, C.; Perez-Mato, J. M.; Wondratschek, H. *Acta Crystallogr., Sect. A: Found. Crystallogr.* **2006**, *62*, 115–128.

(28) Aroyo, M. I.; Perez-Mato, J. M.; Capillas, C.; Kroumova, E.; Ivantchev, S.; Madariaga, G.; Kirov, A.; Wondratschek, H. *Z. Kristallogr.* **2006**, *221*(1), 15–27.

(29) Ling, C. D.; Avdeev, M.; Aivazian, K. *Acta Crystallogr., Sect. B: Struct. Sci.* **2007**, *63*, 584–588.

Table 2. Structural Details for the Subcell of γ-$Ba_4Ta_2O_9$ at 1270 K, from Rietveld Refinement against NPD Data (SPODI, λ = 1.5482 Å)[a]

atom	x (a) [Å]	y (b) [Å]	z (c) [Å]	$100U_{11}$ [Å^2]	$100U_{22}$ [Å^2]	$100U_{33}$ [Å^2]	$100U_{12}$ [Å^2]	$100U_{13}$ [Å^2]	$100U_{23}$ [Å^2]
Ba1	0	0	1/4	7.0(3)	7.0(3)	6.1(4)	3.49(13)	0	0
Ba2	1/3	2/3	0.1193(4)	6.8(2)	6.8(2)	17.1(6)	3.40(11)	0	0
Ba3	0	0	0	6.8(3)	6.8(3)	4.1(4)	3.41(13)	0	0
Ta2	1/3	2/3	0.84260(19)	4.00(10)	4.00(10)	6.5(2)	2.00(5)	0	0
O1	0.5433(14)	0.0459(7)	1/4	8.9(5)	4.2(2)	11.7(4)	2.5(4)	0	0
O2	0.7831(10)	0.6389(6)	0.1045(2)	16.3(5)	8.9(2)	14.5(3)	5.7(3)	2.8(4)	5.7(2)

[a] Space group: hexagonal $P6_3/m$ (No. 176); a = 6.1885(2) Å and c = 16.1277(9) Å. Overall powder R-factors: R_p = 0.0332, wR_p = 0.0463, $R(F^2)$ = 0.1260.

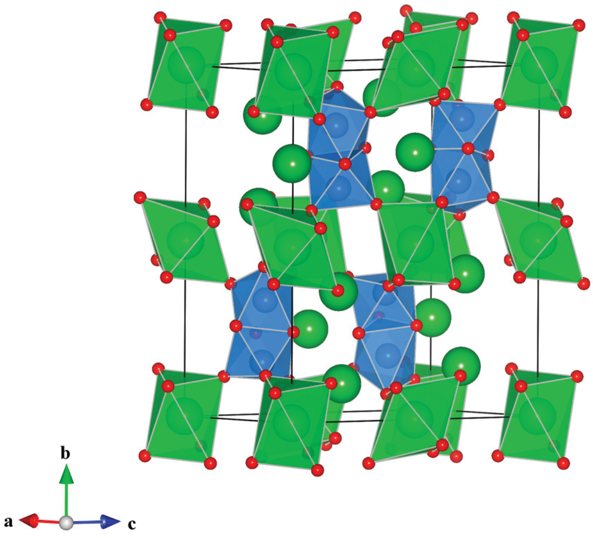

Figure 10. Structure of γ-$Ba_4Ta_2O_9$ at room temperature in $P2_1/c$ space group symmetry, Rietveld-refined against NPD (Echidna) data. Ba atoms are green, Ta atoms are blue, and O atoms are red.

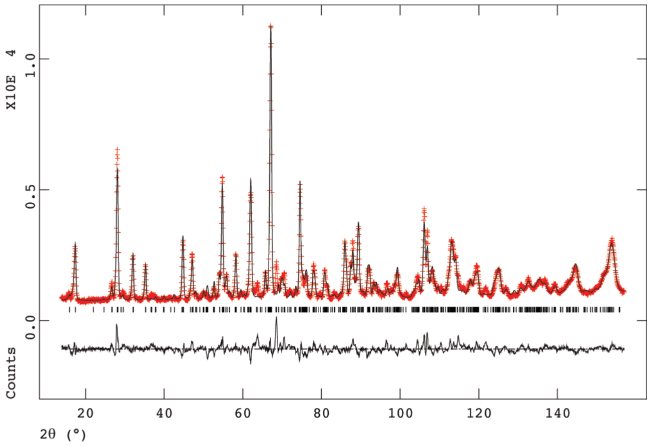

Figure 11. Observed (crosses), calculated (solid line), and difference (below) NPD (Echidna, λ = 2.4395 Å) profiles for the final Rietveld refinement of γ-$Ba_4Ta_2O_9$ in $P2_1/c$ at room temperature.

Table 3. Structural Details for γ-$Ba_4Ta_2O_9$ at Room Temperature from Rietveld Refinement against NPD Data (Echidna, λ = 2.4395 Å)[a]

atom	x (a) [Å]	y (b) [Å]	z (c) [Å]	$100U_{iso}$ [Å^2]
Ba1_1	0.009(4)	0.7387(10)	0.000(2)	$2.0(2)^1$
Ba2_1	0.663(4)	0.9017(9)	0.651(2)	$2.0(2)^1$
Ba2_2	0.661(4)	0.8613(8)	0.164(2)	$2.0(2)^1$
Ba3_1	0.0	0.0	0.0	$2.0(2)^1$
Ba3_2	0.0	0.0	0.5	$2.0(2)^1$
Ta1_1	0.641(3)	0.1658(7)	0.6699(17)	$2.5(2)^2$
Ta1_2	0.685(3)	0.1560(7)	0.1770(16)	$2.5(2)^2$
O1_1	0.441(3)	0.7346(10)	−0.0151(15)	$2.2(1)^3$
O1_2	0.482(3)	0.2452(10)	0.2154(15)	$2.2(1)^3$
O1_3	0.031(3)	0.7327(9)	0.2254(16)	$2.2(1)^3$
O2_1	0.258(3)	0.906(10)	0.1801(16)	$2.2(1)^3$
O2_2	0.194(4)	0.9026(8)	0.6603(19)	$2.2(1)^3$
O2_3	0.905(3)	0.3765(10)	0.1436(13)	$2.2(1)^3$
O2_4	0.877(3)	0.3868(9)	0.6059(16)	$2.2(1)^3$
O2_5	0.652(3)	0.8733(9)	0.9552(18)	$2.2(1)^3$
O2_6	0.602(3)	0.9366(9)	0.4405(16)	$2.2(1)^3$

[a] Space group: hexagonal $P2_1/c$ (No. 14); a = 6.1106(4) Å, b = 16.1109(8) Å, c = 12.2127(10) Å, and β = 120.332(3)°. Overall powder R-factors: R_p = 0.0643, wR_p = 0.0880, $R(F^2)$ = 0.1072. Superscript symbols indicate constraints.

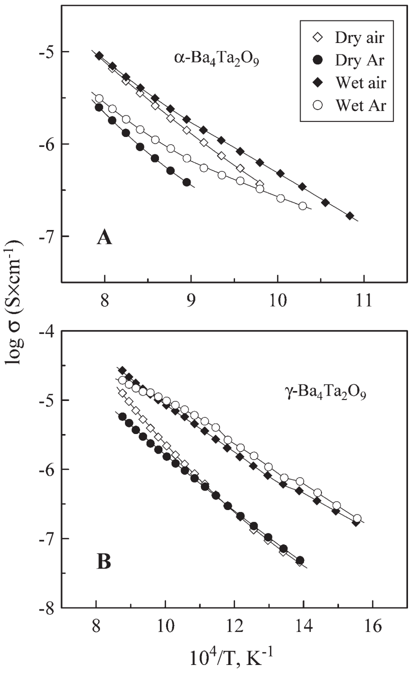

Figure 12. Temperature dependencies of the total conductivity of $Ba_4Ta_2O_9$ ceramics in different atmospheres. All data were collected on cooling in flowing gases. The water vapor partial pressures are ~50 Pa for the dry gases and 3.5 kPa for the wet atmospheres.

At high temperatures and in dry atmospheres, the role of mixed oxygen-ionic and p-type electronic transport seems to increase, as reflected in the rising activation energy and greater effect of the partial pressure of oxygen.

The increasing role of mixed oxygen-ionic and p-type electronic transport at higher temperatures is confirmed by the ionic transference numbers determined by the EMF method and shown in Figure 13. Under oxidizing dry conditions, γ-$Ba_4Ta_2O_9$ (similar to α-$Ba_4Nb_2O_9$[14]) is a mixed oxygen-ionic and p-type electronic conductor. In both cases, the ionic contribution is < 25% and decreases as the temperature increases, because the hole conductivity activation energy is considerably higher (140−170 kJ/mol).

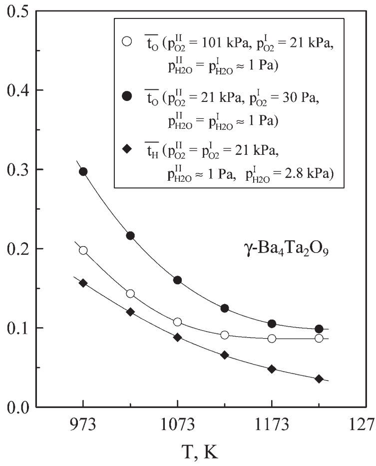

Figure 13. Oxygen-ion and proton transference numbers of γ-$Ba_4Ta_2O_9$ in dried and wet atmospheres. Experimental conditions are given in the legend inside the figure.

Discussion

The most surprising result encountered in this study is the observation that $Ba_4Ta_2O_9$ absorbs more water than $Ba_4Nb_2O_9$ (recall Figure 4). Specifically, α-$Ba_4Ta_2O_9$ hydrates to approximately twice the extent of α-$Ba_4Nb_2O_9$; and, even if the initial mass loss below ~400 K is assumed to be surface water, γ-$Ba_4Ta_2O_9$ hydrates to a significantly greater extent than γ-$Ba_4Nb_2O_9$. In the case of the low-temperature α phases, which are isostructural, this must be due to the greater polarizability of Ta^{5+} vs Nb^{5+}, despite the fact that Ta^{5+} and Nb^{5+} are generally considered to have identical effective ionic radii[30] in 6-fold coordination (0.64 Å). This is tentatively supported by the fact that the unit-cell volume per formula unit for α-$Ba_4Ta_2O_9$ is 0.34% larger than for α-$Ba_4Nb_2O_9$ (258.10(3) vs 257.23(2) $Å^3$, as determined by laboratory XRD at room temperature).

The high-temperature γ phases both have larger equivalent unit cells than their corresponding α phases, also in agreement with their relatively greater hydration. However, comparing the γ phases to each other, the equivalent unit cell volume per formula unit for γ-$Ba_4Ta_2O_9$ is actually 0.47% smaller than for γ-$Ba_4Nb_2O_9$ (260.68(7) $Å^3$ versus 261.90(5) $Å^3$, as determined by laboratory XRD at room temperature), despite being more hydrated. This discrepancy is explained by their different crystal structures. In γ-$Ba_4Nb_2O_9$, protons (hydroxide ions) occupy ordered positions in 2D layers within the structure, along with NbO_4 and NbO_5 polyhedra that do not share coordinating O^{2-} ions with the alternating layers of Nb_2O_9 octahedral dimers. Therefore, the lattice can expand in an "accordion" fashion upon hydration. However, the ordered hydration process in γ-$Ba_4Nb_2O_9$ also has the effect of limiting it to $^1/_3H_2O$ per formula unit. Lattice expansion is much more constrained in γ-$Ba_4Ta_2O_9$, because the layers of Ta_2O_9 octahedral dimers do share coordinating O^{2-} ions with the alternating layers of BaO_6 octahedra; however, the resulting disordered hydration process is not limited by stoichiometry, increasing significantly beyond $^1/_3H_2O$ per formula unit.

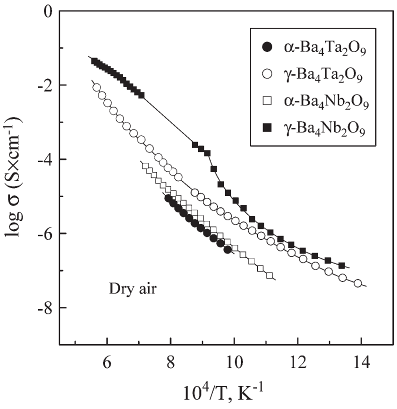

Figure 14. Comparison of the total conductivity of $Ba_4Ta_2O_9$ and $Ba_4Nb_2O_9$ ceramics in dry air, p_{H_2O} = 50 Pa. The data below 1273 K were collected in the cooling regime via AC impedance spectroscopy. The data in the high-temperature range (above ~1273 K) were obtained upon heating via the four-probe DC method.

The second surprising result of this study is that γ-$Ba_4Ta_2O_9$ seems to be more stable than γ-$Ba_4Nb_2O_9$ below the $\alpha \rightarrow \gamma$ transition temperatures. The quenched niobate reverts to the α form over the course of a few hours above 1000 K, but the quenched tantalate does not. This raises the question of why the niobate does not also adopt the 6H-perovskite structure at high temperature. It seems that these compounds are so close to the maximum size difference between B-site cations that can be accommodated in a 6H-perovskite (the effective ionic radii of Ba^{2+}, Ta^{2+} and Nb^{5+} in 6-fold coordination are 1.35, 0.64, and 0.64 Å, respectively) that the greater tolerance of Nb^{5+} for reduced coordination numbers makes the novel γ-$Ba_4Nb_2O_9$ structure a thermodynamically more stable option at high temperatures.

The uniqueness of γ-$Ba_4Nb_2O_9$, with its ordered proton (hydroxide) sites and relatively independent layers, is also shown in the total conductivity data in Figure 14. These data show that γ-$Ba_4Nb_2O_9$ has significantly higher conductivity and behaves quite differently to γ-$Ba_4Ta_2O_9$, α-$Ba_4Nb_2O_9$, and α-$Ba_4Ta_2O_9$. Higher ionic mobility of γ-$Ba_4Nb_2O_9$ may also explain its lower kinetic stability, with respect to γ-$Ba_4Ta_2O_9$ below 1370–1400 K, when both compounds become thermodynamically metastable. The absence of any crystallographic evidence for ordered proton or oxide ion defects in α-$Ba_4(Nb,Ta)_2O_9$ and γ-$Ba_4Ta_2O_9$ means that the protonic and oxide ionic conduction mechanisms in these compounds can only be speculated upon at this stage. In the α phases, it seems plausible that protons and OH^- ions from absorbed water occupy the large voids along the *z*-axis between $(Nb,Ta)_2O_9$ octahedral dimers, hydrogen bonding to the top and bottom faces of the dimers; and in the low-temperature form of γ-$Ba_4Ta_2O_9$, the distortions on the top and bottom faces of the Ta_2O_9 dimers (see Figure 10) could be artifacts of the presence of protons close to those faces. However, a dedicated

---

(30) Shannon, R. D. *Acta Crystallogr., Sect. A: Cryst. Phys., Diffr., Theor. Gen. Crystallogr.* **1976**, *32*(SEP1), 751–767.

dynamics study using experimental (spectroscopic) and *ab initio* computational methods will be needed to explore these possibilities further.

The 6H-perovskite structure of γ-$Ba_4Ta_2O_9$ can be directly compared to that of $Ba_3SrTa_2O_9$ (and $Ba_3SrNb_2O_9$). The size mismatch between Sr^{2+} (1.18 Å in 6-fold coordination) and Ta^{5+}/Nb^{5+} is accommodated by octahedral rotations about the *c*-axis, which reduce the symmetry from ideal $P6_3/mmc$ to $P6_3/m$ at room temperature. The even-greater size mismatch in γ-$Ba_4Ta_2O_9$ leads to further distortions that reduce the symmetry to $P2_1/c$. To the best of our knowledge, this is the only example of this symmetry path being followed as far down as monoclinic in a 6H-perovskite. The other relevant comparison is to $Ba_4Sb_2O_9$, which features an even greater size mismatch between B-site cations—the effective ionic radii of Sb^{5+} in 6-fold coordination is 0.60 Å—but adopts the ideal 6H-perovskite structure in $P6_3/mmc$ space group symmetry above ~600 K.[25,29] The size mismatch in $Ba_4Sb_2O_9$ is too great to be accommodated by any coherent symmetry-reducing distortions, and below this temperature, it decomposes. In this case, the question is why $Ba_4Sb_2O_9$ does not adopt an $Sr_4Ru_2O_9$ structure type, such as α-$Ba_4Ta_2O_9$ and α-$Ba_4Nb_2O_9$. This could be due to variations in metal−metal bond strengths within M_2O_6 dimers as a function of temperature and M; however, developing that hypothesis would require a detailed theoretical investigation that is beyond the scope of this work.

Finally, the relatively low level of mixed conductivity in $Ba_4Ta_2O_9$ and $Ba_4Nb_2O_9$ makes it impossible to envisage their applications in the energy-conversion devices, such as fuel cells or dense ceramic membranes for gas separation. At the same time, both ionic and *p*-type electronic conductivities can be substantially increased by aliovalent doping, enabling one to stabilize the high-temperature polymorphs down to room temperature and to increase defect concentrations. Also, the large water-absorption capacity, the combination of highly basic and acidic components in the lattice, and the p_{H_2O}-dependent transport properties of these materials may be of significant interest for the development of (de)hydration catalysts and thin-film humidity sensors operating in the intermediate-temperature range.

Conclusions

Low-temperature α-$Ba_4Ta_2O_9$ is isostructural with α-$Ba_4Nb_2O_9$, adopting the $Sr_4Ru_2O_9$ structure type. However, high-temperature γ-$Ba_4Ta_2O_9$ (found above 1400 K) is not isostructural with γ-$Ba_4Nb_2O_9$; rather, it adopts a distorted $P6_3/m$ 6H-perovskite structure type analogous to that of $Ba_3SrTa_2O_9$. On quenching below 1400 K, the symmetry of γ-$Ba_4Ta_2O_9$ is reduced from hexagonal $P6_3/m$ to monoclinic $P2_1/c$ at ~900 K. Despite the extremely large size mismatch between B-site cations Ba^{2+} and Ta^{5+}, the monoclinically distorted room-temperature form of γ-$Ba_4Ta_2O_9$ appears to be quite stable, in contrast to the quenched 6H-perovskite $Ba_4Sb_2O_9$ which largely decomposes below ~600 K.[25,29]

Both α and γ phases absorb significant amounts of water below ~950 K, hydrating to an even-greater extent than the corresponding phases of $Ba_4Nb_2O_9$. However, there is no evidence for ordered hydration of the type observed in γ-$Ba_4Nb_2O_9$. Both phases show mixed-proton, oxide-ionic, and electronic conduction. Protonic conduction dominates in the hydrated phases, with oxide ionic and electronic conduction playing increasingly important roles upon dehydration.[31−33]

Acknowledgment. This work was supported by the Australian Research Council−Discovery Projects (No. DP0666465) and the FCT, Portugal (Project No. PTDC/CTM/64357/2006). Travel to the FRM-II Research Reactor for NPD data collection was supported by Australian Institute of Nuclear Science and Engineering (AINSE).

Supporting Information Available: CIF files for α-$Ba_4Ta_2O_9$ (Rietveld-refined against NPD data at 300 K), γ-$Ba_4Ta_2O_9$ (Rietveld-refined against NPD data at 1270 K), and γ-$Ba_4Ta_2O_9$ (Rietveld-refined against NPD data at 300 K). This material is available free of charge via the Internet at http://pubs.acs.org.

---

(31) Ramirez, E. G. U.S. Patent 4,376,732, March 15, **1983**.
(32) Tanabe, K. *Catal. Today* **1990**, *8*, 1–11.
(33) Hashizume, T.; Saiki, A.; Terayama, K.; Torishima, T. *Ceram. Trans.* **2006**, *196*, 407–413.